# Simultaneous extraction of carotid artery intima-media interfaces in ultrasound images: assessment of wall thickness temporal variation during the cardiac cycle

**Guillaume Zahnd[1,2], Maciej Orkisz[2], André Sérusclat[3], Philippe Moulin[4,5], Didier Vray[2]**

[1]Biomedical Imaging Group Rotterdam, Departments of Radiology & Medical Informatics, Erasmus MC, P.O. Box 2040, 3000 CA Rotterdam, The Netherlands (g.zahnd@erasmusmc.nl)
[2]Université de Lyon, CREATIS; CNRS UMR 5220; INSERM U1044; INSA-Lyon; Université Lyon 1, France
[3]Department of Radiology, Louis Pradel Hospital, Lyon, France
[4]Department of Endocrinology, Louis Pradel Hospital; Hospices Civils de Lyon; Université Lyon 1, Lyon, France
[5]INSERM UMR 1060, Lyon, France

***Manuscript published in International Journal of Computer Assisted Radiology and Surgery (DOI: 10.1007/s11548-013-0945-0). The final version of the paper is available at: http://link.springer.com/article/10.1007%2Fs11548-013-0945-0***

## Abstract

*Objectives.* The aim of this work is to present and evaluate a novel segmentation method for localizing the contours of the intima–media complex in the carotid artery wall through longitudinal ultrasound B-mode imaging. The method is used to investigate the association between atherosclerosis risk factors and the cyclic variation of the intima–media thickness during the heart beat.
*Methods.* The framework introduced is based on two main features. The first is a simultaneous extraction of both the lumen–intima and the media–adventitia interfaces, using the combination of an original shape-adapted filter-bank and a specific dynamic programming scheme. The second is an innovative spatial transformation that eases the extraction of skewed and curved contours, and exploits the result from the previous image as *a priori* information, when processing the current image. The intima–media thickness is automatically derived from the estimated contours for each time step during the cardiac cycle. Our method was evaluated *in vivo* on 57 healthy volunteers and 25 patients at high cardiovascular risk. Reference contours were generated for each subject by averaging the tracings performed by three experienced observers.
*Results.* Segmentation errors were $29 \pm 27\,\mu$m for the lumen–intima interface, $42 \pm 38\,\mu$m for the media–adventitia interface, and $22 \pm 16\,\mu$m for the intima–media thickness. This uncertainty was similar to inter- and intra-observer variability. Furthermore, the amplitude of the temporal variation in thickness of the intima–media layers during the cardiac cycle was significantly higher in at-risk patients compared to healthy volunteers ($79 \pm 36\,\mu$m *vs* $64 \pm 26\,\mu$m, $p = 0.032$).
*Conclusion.* The method proposed may provide a relevant diagnostic aid for atherosclerosis screening in clinical studies.

**Keywords:** *Atherosclerosis; Carotid artery; Contour segmentation; Dynamic programming; Intima–media thickness; Shape-adapted filter*

# 1 Introduction

## 1.1 Clinical context

Cardiovascular disease remains the major cause of mortality and morbidity in industrialized countries. During the atherosclerosis process, clinical events such as myocardial infarction and stroke are caused by rupture of atheromatous plaque [40]. Several alterations of the blood vessel properties can already be observed at the early stage of the pathology, such as endothelial dysfunction, vascular remodeling, as well as arterial thickening and stiffening [7, 22, 34]. It has also recently been demonstrated that preventive care (*i.e.*, treatment of arteriosclerosis and atherosclerosis at early stages) can dramatically reduce the mortality rate related to cardiovascular disease [17, 47]. Therefore, early detection of accelerated vascular aging is a major clinical issue.

Carotid intima–media thickness (IMT) has been demonstrated to be strongly correlated with cardiovascular disease by several previous studies [1, 4, 6]. This parameter is considered an established marker of atherosclerosis [26, 33]. A recent *in vivo* investigation, carried out with ultrasound (US) B-mode imaging, has shown that the IMT actually undergoes a reproducible compression–decompression phenomenon during the cardiac cycle [42], namely the IMT is maximal at the end of diastole and minimal during systole. Further clinical studies have considered the amplitude of this phenomenon, henceforth denoted as $\mathcal{A}_{\mathrm{IMT}}$, and demonstrated a positive correlation with cardiovascular risk factors [5, 27, 35, 36]. According to these findings, the $\mathcal{A}_{\mathrm{IMT}}$ parameter is likely to be a novel and relevant marker to assess atherosclerosis and may be useful in screening vulnerable patients.

## 1.2 Carotid wall segmentation in US B-mode imaging

A wide variety of methods have been proposed to segment the common carotid artery (CCA) wall layers in two-dimensional (2D) US B-mode images (Fig. 1). Many of them aimed at quantifying the IMT, but previous work can be mentioned that exploited contour segmentation within a motion-estimation framework dedicated to track the 2D motion of the wall tissues [14, 28, 50]. The first category of methods is exclusively based on image features. In this context, an edge-tracking method using intensity gradient was introduced in [41], and an approach based on envelope intensity thresholding was proposed in [10]. Other studies also introduced different methods to exploit the local statistics of the image, using a mixture of Nakagami distributions and stochastic optimization [14], a multiscale anisotropic barycenter based on statistical filtering [15], and a fuzzy K-means classifier [31]. A second category of methods involves, in addition to image features, a fitting scheme designed to converge towards the optimal solution. In this context, several teams have proposed different implementations of the active contours framework [9, 13, 25]. Moreover, dynamic programming approaches have also been proposed, based on fuzzy expression forms representing image features and geometrical characteristics of vessel interfaces [24], smooth intensity thresholding surfaces and geometric snakes [37], directional Haar-like filter [23], and dual contour detection [8, 50]. A detailed state-of-the-art review covering the field of CCA segmentation in US B-mode imaging is provided in [30].

The above-mentioned compression–decompression of the IMT during the cardiac cycle has also been assessed by various teams. In these studies, the segmentation of the intima–media

complex was carried out sequentially, as opposed to the segmentation of a single image. The temporal variation of the IMT value was then derived from the results of the contour extraction at different time steps. Towards this objective, four main strategies have been proposed to perform the segmentation process. The first type only involves two different specific time steps, namely the end-diastole and the systole, mostly featuring approaches based on manual tracing [35, 36]. The second type consists in segmenting each frame of the sequence independently, *i.e.*, without exploiting any relation between two consecutive time steps. Different approaches have been introduced in this context, such as a method based on the Hough transform [19], detection of the maximum intensity echoes [11, 32], active contours [20], manual segmentation [39], dual line detection [44], finite element modeling [46], and phase change detection in radiofrequency data [45]. The third type is based on the temporal consistency of the sequence, and segments all consecutive frames by exploiting the results from the previous operation as an input for the current operation. Fewer studies have investigated this field, among which are methods based on statistical filtering with region update [38] and wall tracking by adaptive normalized correlation [21]. Finally, a fourth type of technique is segmentation using a surface fitting approach in a 2D+t volume, as presented in [28].
Among the pitfalls that may hamper contour segmentation of the carotid artery in US B-mode imaging, the following are the most commonly encountered. The organ anatomy itself represents a difficulty. Indeed, the two interfaces of the intima–media complex to be segmented are very close to each other, and have a similar pattern [48]. For that reason, methods based on a single characteristic (*i.e.*, intensity gradient only) are often jeopardized. Furthermore, the US modality, despite its numerous advantages, also presents a few drawbacks that must be taken into consideration, such as poorly contrasted interfaces, a rather low signal-to-noise ratio (SNR), and weak echoes. Therefore, methods that are based on a single feature with no shape constraint or that perform the segmentation locally (*i.e.*, column by column in a 2D image), are less likely to extract realistic and accurate contours. Namely, frequent failures occur, where one (or both) interface(s) locally present(s) weak contrast. Additionally, when working on clinical datasets, great variability in both image quality and anatomic geometry can generally be observed between images of different subjects.

## 1.3 Objectives and contributions

The objective of the present article is twofold. First, we introduce a novel segmentation framework that simultaneously extracts both lumen–intima (LI) and media–adventitia (MA) contours of the CCA *in vivo* in US B-mode sequences. Second, we investigate $\mathcal{A}_{\mathrm{IMT}}$, corresponding to the temporal variation of the intima–media thickness during the cardiac cycle, using the previously segmented contours. Let us note that the framework introduced was specifically designed to assess so-called "normal" carotid arteries, in which alteration of the wall by the formation of an atheromatous plaque (if any) is not yet perceptible, in the context of screening vulnerable patients who are prone to developing atherosclerosis [7].
The main methodological contribution of the work reported in this article is a combination of a specific filter bank and an appropriate dynamic programming strategy, to cope with discontinuities due to contrast drop locally observed along the interfaces. Furthermore, to manage variable geometry, *i.e.*, arterial wall skewed and/or curved in the image plane, we devised a local spatial transform that makes the interfaces nearly horizontal. Additionally, when processing a whole sequence to assess the temporal variation of the wall location and thickness, the results obtained for the previous frame are used as *a priori* information to segment the current frame.
The accuracy of the present segmentation method was evaluated *in vivo*, on the full exploitable

width of the carotid distal wall of 82 subjects (57 healthy volunteers and 25 patients at high cardiovascular risk likely to develop cardiovascular disease) in US B-mode imaging. All measurements and analyses were conducted on the distal wall of the CCA, to take advantage of a better echogenicity [48]. When comparing the results of this novel approach with those obtained manually by three independent experts, the accuracy of our method compared to the reference was similar to inter- and intra-observer variability, and the reproducibility of our method was systematically greater. Finally, we investigated the clinical relevance of the $\mathcal{A}_{\mathrm{IMT}}$ parameter, *i.e.*, the amplitude of the compression–decompression phenomenon of the IMT during the heart beat, by comparing the results between healthy volunteers and at-risk patients. Statistical analysis showed that $\mathcal{A}_{\mathrm{IMT}}$ was significantly increased in at-risk patients, which tends to confirm that this parameter could constitute a relevant marker for screening vulnerable patients [5, 27, 35, 36].

# 2 Material and Methods

The introduced method is semi-automatic and relies on a quick and simple interactive initialization phase (Fig. 2), aiming to increase the overall robustness by avoiding errors that may be introduced by fully automatic procedures. The subsequent segmentation approach (Fig. 3) is characterized by the extraction of a single skeleton line and is based on the estimation of a local thickness parameter that simultaneously define the location of both LI and MA interfaces. This method is sequential, *i.e.*, all frames of the sequence are successively processed and the results from the previous operation performed at time step $(n-1)$ are exploited as *a priori* information for the current operation at time step $n$. The temporal variation of the IMT during the cardiac cycle is thus assessed, and the $\mathcal{A}_{\mathrm{IMT}}$ parameter is calculated as the difference between the diastolic and systolic estimated IMT (*i.e.*, the maximal and minimal IMT values, respectively).

## 2.1 Initialization

Manual initialization is performed in the first frame $\mathcal{I}(1)$ of the sequence. This phase involves three consecutive steps (see Figure 2 for a graphical sketch), as described below.

- Firstly, a region of interest (ROI), denoted $\mathcal{I}_W$, is defined by the user. Since the borders of the image sometimes show blur, low echoes and/or high noise, these poor-quality parts are clipped out, if necessary. The height of the ROI remains equal to the full image height, whereas its width $W$ is defined by clicking two points that indicate the left and right limits, beyond which the LI and MA interfaces cannot be perceived.
- Then, the user provides a rough initial estimate of the IMT by positioning two radially aligned points on the LI and the MA interfaces.
- Finally, an even rougher delineation of the skeleton is given by positioning three points, located within the intima–media complex on the left, middle, and right sides of the ROI.

The initialization parameters are then stored and the full sequence is automatically processed, as described below.

## 2.2 Segmentation framework

**Spatial transformation $T$** The aim of the transformation $T$ is to generate a sub-image $\mathcal{I}_T$ in which the anatomical interfaces become nearly horizontal (Fig. 3a, b), with two objectives: (1)

managing images where the artery segment of interest is tilted or curved and (2) keeping track of the radial displacement of the wall. We thus overcome the limitation of several existing methods [15, 19] that require careful acquisition such that the interfaces of interest are horizontal. At first, the skeleton from the frame $\mathcal{I}(n-1)$ is mapped onto the frame $\mathcal{I}(n)$ (when $n=1$, the approximate skeleton defined by the three points during the initialization step is used)[1]. Then, the transformed image $\mathcal{I}_T$ is created by applying the spatial transformation $T$ on the original $\mathcal{I}_W$ sub-image, such that:

$$\mathcal{I}_T = T(\mathcal{I}_W). \tag{1}$$

The transformation $T$ consists in selecting $L$ pixels above and below the skeleton in $\mathcal{I}_W$ (Fig. 4). To obtain greater precision in the segmentation process, the image is interpolated by a factor of 10 in the radial direction. The interpolation was bilinear and achieved in Matlab (Matlab 7.13, The MathWorks Inc., Natick, MA, USA, 2011) with the function *interp2*.

**Shape-adapted filter $\mathcal{H}_\Delta$** The aim of this novel original shape-adapted filter is to provide strong responses within the intima–media complex at points located mid-way between the contours to be extracted, together with a local estimation of the distance between them (IMT). We introduce a convolution operator $\mathcal{H}_\Delta$ that models the characteristic structure of the arterial wall observed in US images (Fig. 1), representing the two transitions (*i.e.*, the LI and MA interfaces) between zones with different echogenicity:

$$\mathcal{H}_\Delta = \pm G' * \mathcal{M}_\Delta. \tag{2}$$

Here, $(*)$ is the convolution operator, $G'$ is the first derivative of a Gaussian of standard deviation $\sigma$ and of length $l$ (representing the intensity gradient between two layers), and $\mathcal{M}_\Delta$ a pair of Diracs separated by $\Delta$, with $\Delta \geq l$ (representing the typical double-line pattern of the interfaces). The $\pm$ sign corresponds to the gradient orientation, and is determined according to the processed wall, *i.e.*, it is negative for the distal wall used in this study, and would be positive if the proximal wall was used. To prepare a front-propagation step (see next paragraph), a velocity map $\mathrm{F}_\Delta$ is then built:

$$\mathrm{F}_\Delta = \mathcal{H}_\Delta * \mathcal{I}_T, \tag{3}$$

with $\mathcal{H}_\Delta$ applied column-wise. The largest values in $\mathrm{F}_\Delta$, with $\Delta$ equal to the local IMT, represent the points most likely to belong to the skeleton (Fig. 3c). Although the IMT can be considered as almost constant, since this study involves the detection of the pathology at an early stage with no perceptible atheromatous plaques, this thickness is subject to tiny changes during the heart cycle [42]. To manage these minute variations that can occur both spatially within a single image and temporally between two consecutive images, actually a set of $K$ (odd number) filters $\mathcal{H}_{\Delta^k}$ is applied on $\mathcal{I}_T$ to build $K$ maps $\mathrm{F}_{\Delta^k}$ (Fig. 3c). The $K$ tentative values of the local IMT are defined as follows:

$$\Delta^k = \Delta(n-1) + k\delta, \qquad k \in \mathcal{K} \equiv \{-\frac{K-1}{2}, \dots 0, \dots \frac{K-1}{2}\}, \tag{4}$$

where $\delta$ is an increment corresponding to the minimal IMT variation investigated and $\Delta(n-1)$ is the IMT value estimated in $\mathcal{I}(n-1)$. When $n=1$, the approximate IMT value defined by the two points during the initialization step is used. Then a single velocity map F is generated

[1] We drop $n$ to simplify the notations, when it is not confusing, since all the subsequent steps in this section are explained on the same time-point $n$.

pixel-by-pixel by independently selecting, for each point $(x, y)$, the highest $\mathrm{F}_{\Delta^k}(x, y)$ value among the corresponding candidates from all the $K$ maps (Fig. 3d):

$$\forall (x, y), \mathrm{F}(x, y) = \max_{k \in \mathcal{K}} \left\{ \mathrm{F}_{\Delta^k}(x, y) \right\}, \tag{5}$$

while storing the corresponding local values of $\Delta^k, k = \mathrm{argmax}_{k \in \mathcal{K}} \left\{ \mathrm{F}_{\Delta^k}(x, y) \right\}$. Finally, a cost map C is generated, where the points most likely to represent the skeleton correspond to the positions with the lowest values of C (Fig. 3e):

$$\mathrm{C} = \exp(-\mathrm{F}). \tag{6}$$

**Dynamic programming** Given that US images are noisy, contrasts are inhomogeneous and Equation 5 is evaluated independently in each column, the locations of thus found maxima do not form a smooth path. A smoothness constraint is therefore introduced and a globally optimal solution (minimum-cost path) is sought, while the cost map is used as a data-attachment term. Dynamic programming is generally used to implement optimization algorithms in combinatorial analysis [2]. The aim of this strategy is to determine, using a global approach, the optimal solution among all possible combinations, overcoming a costly full-search. The general principle, upon which this approach is based, consists in a successive resolution of sub-problems, whose combined solutions eventually optimally solve the initial problem. In the present case, the actual problem is to find the optimal path that defines the skeleton located mid-way between the LI and MA contours, corresponding to the lowest cumulative cost $\mathcal{C}$ (highest responses of the filter $\mathcal{H}$). First, a seed point $\mathbf{s} = (x_s, y_s)$ is automatically determined by seeking the center of the longest valley in C, that is to say the longest continuous segment of minimal values in C. The continuity notion is defined here by a maximal vertical variation of $\pm$ 10 pixels (which would correspond to $\pm$ 1 pixel in the non-interpolated original image) between two adjacent columns. From the seed point $\mathbf{s}$, a specific front propagation scheme is then run in order to build a cumulative cost map $\mathcal{C}$ (Fig. 3f). The front propagation scheme introduced is adapted from the fast-marching methodology [12, 43] to provide a unidirectional (*i.e.*, across the image width) path, favoring the propagation along the valleys in C while penalizing the non-horizontal displacements. The initial value is set as:

$$\mathcal{C}(x_s, y_s) = \mathrm{C}(x_s, y_s). \tag{7}$$

Then, from the seed $\mathbf{s}$ to the left and right borders, the map $\mathcal{C}$ is iteratively built using the following relation:

$$\mathcal{C}(x + dx, y) = \min_{dy \in \{-10, \ldots 0, \ldots 10\}} \left\{ \mathcal{C}(x, y + dy) + \mathrm{C}(x + dx, y) \sqrt{1 + \left( \frac{dy}{10} \right)^2} \right\}, \tag{8}$$

with $dx = -1$ when $x < x_s$ (*i.e.*, on the left side of the seed) and $dx = +1$ when $x > x_s$ (*i.e.*, on the right side of the seed). In Equation 8, $\mathcal{C}(x, y + dy)$ corresponds to the already solved sub-problem term (*i.e.*, the previously calculated value of the map $\mathcal{C}$), $\mathrm{C}(x + dx, y)$ is the image data term at the current point (*i.e.*, the value C inferred from the result of the dual interface filtering), and $\sqrt{1 + \left( \frac{dy}{10} \right)^2}$ is a shape constraint term (*i.e.*, the penalty calculated as the Euclidean distance to the candidate point). The latter term penalizes the vertical "yaw" $dy$, whose variation interval corresponds to $\pm 1$ pixel in the original non-interpolated image. Finally, on both the left and right borders of the image, the point with the minimal cumulative cost is determined and the minimal path is found by back-tracking the decreasing values in the map $\mathcal{C}$ [12] from these border points to the seed $\mathbf{s}$ (Fig. 3g).

**Inverse transformation $T^{-1}$** Finally, the skeleton position is determined by mapping back the optimal path onto the original image $\mathcal{I}(n)$ by the $T^{-1}$ operation. Then the two contours of the intima–media complex are deduced from the skeleton position and from the stored local values of $\Delta^k$ (Fig. 3h). Finally, the IMT $\Delta(n)$ corresponding to the current $n^{\text{th}}$ frame, calculated as the column-wise mean radial distance between the LI and MA contours over the width $W$, is stored for further analysis.

## 2.3 Estimation of the $\mathcal{A}_{\text{IMT}}$ parameter

The $\mathcal{A}_{\text{IMT}}$ parameter, corresponding to the amplitude of the temporal variation in thickness of the intima–media layers, was assessed for each sequence from the segmentation results. From our experience however, the measurement of the IMT temporal variation integrated over the full exploitable width of the image sometimes fails to capture a cyclic and reproducible compression–decompression pattern. Therefore, to assess the tiny temporal changes of the IMT [42], we preferred to integrate the distance between the LI and MA contours over a narrower region ($W = 3\,\text{mm}$). This narrow region was centered on the most contrasted part of the image. We expected that the variations of interest would be homogeneous within such a short artery segment. Curves representing the IMT values thus estimated during several consecutive cardiac cycles were presented to an experienced user together with the corresponding electrocardiograms (ECG). The user, blinded to all clinical information, selected end-diastole and systole of at least two consecutive cardiac cycles. The $\mathcal{A}_{\text{IMT}}$ parameter was first calculated as the end-diastole-to-systole difference in IMT for each cycle, then averaged across the available cycles. The choice of this manual reading instead of a fully-automatic process to determine $\mathcal{A}_{\text{IMT}}$ from the IMT variation curves was motivated by two factors: first, the ECG signal was not available as is, but rather superimposed on the image, and second, this reading operation can be performed very easily and quickly by the user. The drawback of this solution is that it may introduce some user-dependent variability.

## 2.4 Acquisition of in vivo image data

### 2.4.1 Study population

In this study, 82 subjects (57 young healthy volunteers and 25 older patients at high cardiovascular risk, *i.e.*, likely to develop atherosclerosis but with no established cardiovascular disease) were involved. The healthy volunteers were 24 males and 33 females, with an average age of $37.9 \pm 14.1$ years (range, $19 - 63$ years), and pulse pressure of $44 \pm 8$ mmHg. The at-risk patients were 16 males and 9 females, with an average age of $56.2 \pm 10.5$ years (range, $34 - 73$ years), and pulse pressure of $54 \pm 15$ mmHg. All healthy volunteers were cardiovascular risk factor-free (tobacco use, hypercholesterolemia, diabetes, hypertension or particular family history), as assessed by an oral questionnaire. The inclusion criterion for the patient group was the presence of either metabolic syndrome, or type 1 or 2 diabetes, diagnosed at least 1 year before [16]. No other criterion, including clinical characteristics, was used to select these participants. Informed consent was obtained from all participants. The study fulfilled the requirements of our institutional review board as well as the ethics committee.

### 2.4.2 Acquisition of carotid artery ultrasound sequences

All subjects underwent a US examination. A medical scanner (Antares, Siemens, Erlangen, Germany), equipped with a 7.5- to 10-MHz linear array transducer, was used to perform US acquisition. Longitudinal B-mode image sequences of the left CCA were acquired after a

15-min rest, the subjects lying in supine position, with the neck being extended and rotated 45° to the contralateral side. The probe was centered on the CCA, in the longitudinal plane (*i.e.*, along the axis of the artery), positioned 2 cm from the carotid bulb. The absence of atheromatous plaques in the imaged region was systematically assessed by a medical doctor. Temporal sequences of images were acquired, covering on average $2.6 \pm 0.7$ heart beats, with at least two consecutive full cardiac cycles. In order to avoid motion artifacts, the subjects were asked to perform a breath hold and not to swallow during the acquisition. All acquisitions were performed using the following instrumentation settings: the dynamic range was 65 dB, the sequence frame rate was 26 fps, the pixel size in both radial and longitudinal directions was $30\,\mu$m. The recorded scans were stored digitally and transferred to a commercial computer for off-line analysis. No participant was rejected from the study.

## 2.5 Evaluation of the method's accuracy

The segmentation accuracy of the present method was assessed on the entire exploitable width $W$ of the first frame in each sequence. Aiming to quantify the accuracy of our method despite the lack of ground truth inherent to clinical imaging, reference segmentation contours were generated for each sequence by three experienced observers $O_1$, $O_2$ and $O_3$. The observers were specialists in US image modeling, processing and analysis with 5, 23 and 3 years of experience, respectively. First, as the left and/or right borders of the image sometimes show blur, low echoes or high noise, observer $O_1$ was asked to clip out the poor-quality borders, if necessary (Fig. 2), thus defining the $\mathcal{I}_W$ region to be considered. Then, the segmentation method was applied to localize the contours of both LI and MA interfaces. Subsequently, each observer performed the manual segmentation of both interfaces, blinded to the automatic results.

For the first frame of each sequence, the reference contour segmentation was constructed by averaging the results from the three observers, for both interfaces. The corresponding reference IMT (denoted as $\text{IMT}_{REF}$) was calculated as the mean distance between the LI and MA reference contours, over the width $W$ of the ROI.

The method's reproducibility was also assessed. Since some variability could potentially be introduced during the manual initialization phase (Section 2.1). To investigate this impact, our method was applied twice, with observer $O_1$ performing the initialization phase a second time, within the same clipped $\mathcal{I}_W$ region for each sequence. Similarly, intra-observer variability of the manual tracings was also assessed. For this purpose, the manual segmentation was performed twice by observer $O_1$, within the same clipped $\mathcal{I}_W$ region of the first image in each sequence. Finally, the $\mathcal{A}_{\text{IMT}}$ parameter (*i.e.*,the amplitude of the IMT variation), derived from the automated segmentation results, was also assessed twice for each sequence, *viz.*: in a randomized manner and blinded to all clinical information, observer $O_1$ twice located the systole and end-diastole time-points on the resulting IMT curves. All resulting contours were stored for further analysis.

## 2.6 Parameter settings

Our method was applied on all the sequences with the following parameter settings: number of pixels above and below the skeleton used in the transformation $T$, $L = 34$, corresponding to a 1 mm half-height; standard deviation of the Gaussian $G$, $\sigma = 0.35$, corresponding to $10\,\mu$m, and its length $l$ equal to 75% of the approximate IMT provided at the initialization stage; number of possible $\Delta^k$ values of the IMT, $K = 61$, with increment $\delta = 3\,\mu$m, thus leading to a variation range of $\pm 90\,\mu$m around the IMT estimated in the previous frame.

## 2.7 Statistical analysis

The Mann-Whitney U test was used to compare the values of end-diastole IMT, as well as the total amplitude of the IMT variation, $\mathcal{A}_{\mathrm{IMT}}$, during the cardiac cycle, between healthy volunteers and at-risk patients. The value $p < 0.05$ was considered to indicate a statistically significant difference.

To determine the agreement between two repeated measurements, the measurement error was calculated as follows:

$$err = \frac{\sqrt{var}}{m} \times 100\%, \tag{9}$$

with $var$ the within-subject variance and $m$ the average of all measurements [3]. The corresponding intra-class correlation coefficient (ICC) and its 95% confidence interval (CI) were also computed. All statistical analyses were performed using Matlab.

# 3 Results

## 3.1 Contour segmentation

The average width $W$ of the $\mathcal{I}_W$ sub-images was $19 \pm 5\,\mathrm{mm}$ (range, $10 - 29\,\mathrm{mm}$), which corresponds to an average ratio of $80 \pm 20\%$ (range, $41 - 100\%$) of the full width of the images. For all 82 subjects, our segmentation method successfully localized the anatomical interfaces of the wall, and the extracted contours matched the reference contours well. Representative examples of resulting segmented contours, corresponding to subjects with varying image quality, are displayed in Figure 5.

For both LI and MA interfaces, the unitary segmentation error $\epsilon(x)$ was defined as the distance between the reference contour and the estimated contour, in the column $x$ of the image. The IMT estimation error was defined as the difference between the estimated (averaged on $W$ in the given image) IMT and the reference value, $\mathrm{IMT}_{REF}$.

The mean absolute errors ($\pm$ standard deviation) of the segmentation process are displayed in Table 1. These results were calculated by putting together in a single vector all the corresponding unitary segmentation errors, prior to generating the mean absolute error and standard deviation. Let us first note that the errors of our method were of the same order of magnitude as inter- and intra-observer variability, while its variability was significantly smaller than inter- and intra-observer variability.

When analyzing these errors, it is also useful to compare them with the thickness of the segmented tissue, *i.e.*, the IMT. The mean value ($\pm$ standard deviation) of the reference intima–media thickness in all the assessed subjects was $618\,(\pm 152)\,\mu$m. Calculating the ratio between each absolute segmentation error $|\epsilon(x)|$ and the corresponding individual $\mathrm{IMT}_{REF}$, and putting all these ratios together, the mean values ($\pm$ standard deviation) were: $5(\pm 5)\%$ for the LI interface, $7(\pm 7)\%$ for the MA interface, and $4(\pm 3)\%$ for the estimated IMT.

Figure 6 shows a good correlation ($R = 0.985$) between the IMT estimated with our method and the reference. The Bland-Altman plot (Fig. 7) also demonstrates good agreement between the estimated IMT and the reference, with a 95% CI of $51\,\mu$m and a slight over-evaluation of $9\,\mu$m. The details of this bias *versus* the reference for our method, as well as for each observer, are provided in Table 1.

## 3.2 IMT analysis

For each subject, the temporal variation of the IMT was estimated during the entire length of the sequence, over a sub-region of reduced width $W = 3\,\mathrm{mm}$ (Fig. 8). The total number of

analyzed frames in all the sequences considered was 9539, with an average number of $116 \pm 34$ frames per sequence (range, $66 - 194$). Implemented in Matlab, the present method required on average 189 s to segment an entire sequence (*i.e.*, 1.6 s/frame), the initialization phase took less than 20 s. This is to be compared with an average of 162 s/frame to manually trace both interfaces of the intima–media complex.

A cyclic compression–decompression pattern could be observed during the cardiac cycle, as displayed in Figure 9. More precisely, the diastolic IMT was systematically greater than the systolic IMT, namely $662 \pm 148\,\mu$m and $594 \pm 140\,\mu$m, respectively, which corresponds to previous findings reported by different teams [19, 27, 42]. The average amplitude of the thickness variation, $\mathcal{A}_{\mathrm{IMT}}$, was equal to $69 \pm 30\,\mu$m and represented $11 \pm 5\%$ of the estimated end-diastole IMT.

The result of the Mann-Whitney U test demonstrated that the end-diastole IMT value, estimated with our segmentation method, was significantly higher in at-risk patients compared to healthy volunteers ($747 \pm 163\,\mu$m *vs* $573 \pm 103\,\mu$m, $p < 0.0001$), which is in accordance with previous studies [1].

More interestingly, the mean $\mathcal{A}_{\mathrm{IMT}}$ was also significantly higher in at-risk patients compared to healthy volunteers ($79 \pm 36\,\mu$m *vs* $64 \pm 26\,\mu$m, $p = 0.032$), as depicted in Figure 10.

The variability of the $\mathcal{A}_{\mathrm{IMT}}$ parameter measurement due to manual localization of the systole and diastole was 9.7% (Eq. 9), with ICC equal to 0.92 ($95\%\,\mathrm{CI} = 0.88 - 0.95$) and the Pearson correlation coefficient equal to 0.92.

# 4 Discussion and conclusion

The present contour extraction method was successfully applied on 82 subjects, to detect the location of the carotid lumen–intima and media–adventitia interfaces and showed good accuracy. The temporal variation of the IMT presented a cyclic compression–decompression pattern along the heart beat. The amplitude of this compression was found to be significantly increased in at-risk patients compared to healthy controls.

## 4.1 Contour segmentation

Evaluated *in vivo* on images from 82 subjects, the accuracy level of this novel segmentation method was very similar to inter- and intra-observer variability, *i.e.*, the mean absolute distance was approximately one pixel (Table 1), while its reproducibility was much better. Moreover, the accuracy in the at-risk patients was substantially the same as in the healthy volunteers, despite often worse echogenicity of the former. These results demonstrate a certain robustness of our method, as all 82 sequences of the clinical dataset were successfully segmented using the same parameter settings, despite differences in arterial geometry and image quality.

The segmentation of the carotid artery wall has been widely investigated, with the objective of measuring the IMT, the internal diameter, or the plaque volume. According to a recent detailed review [30], the most accurate methods are those proposed in [29] and [14]. The former was reported to quantify the IMT with an average error of $10 \pm 10\,\mu$m, but its inaccuracy in the extraction of the LI and MA interfaces ($35 \pm 32\,\mu$m and $37 \pm 29\,\mu$m, respectively) were very close to ours. The latter approach extracted the respective interfaces with an average error of $21 \pm 12\,\mu$m and $16 \pm 7\,\mu$m, but the IMT accuracy was not reported, so it is hard to determine if the corresponding error was similar, larger or smaller than the errors for each interface separately. Based on the results reported, the present method would rank among the most accurate state-of-the-art approaches. Nevertheless, the pertinence of such comparisons is limited by several differences in the evaluation protocols, such as the distance metric (*e.g.*,

mean absolute distance or polyline distance), ROI (*e.g.*, full width, or limited region), data included (*e.g.*, only healthy volunteers, patients with/without perceptible atheromatous plaques), image characteristics (*e.g.*, spatio-temporal resolution, presence or absence of skewed and curved arterial walls).

A very important difference is related to the reference segmentation. As ground truth is not available in clinical imaging, the reference contours generally are traced by experienced observers, but several experts are necessary to provide an averaged or consensus reference. Nevertheless, as long as different images with contours traced by different experts are used, the evaluation results are also likely to differ slightly. In the present study, each expert introduced a different bias in the contour location, as shown in Table 1: the resulting IMT was overestimated by two of them, similarly to our method, while the third one introduced a large negative bias with regard to the averaged reference. However the amplitude of these errors remained smaller than one pixel. The inter- and intra-observer variability also was on the pixel scale and small in comparison to the IMT. We therefore consider that the averaged contours used in this study constitute a valid reference to evaluate the automated method. Conversely, as the errors of our method are within inter- and intra-observer variability, the method can be considered as accurate.

Other criteria that may influence the results, when comparing various methods are the degree of automation and the processing time. According to the survey in [30], the fully automatic methods are substantially less accurate except the one presented in [29]. Our method involves a manual initialization in the first frame of the sequence, aiming to increase the overall accuracy by discarding, when necessary, the regions with poor image quality. This phase takes not more than 20 s, and the remainder of the sequence is processed automatically. The computation time is directly proportional to the ROI width, as well as to the number of frames in the sequence. In our experiments, where the average ROI size was equal to 80% of the image size, our method performed the segmentation 100 times faster than the experts. The processing speed can be improved by using a compiled programming language and by optimizing the implementation.

## 4.2 IMT variation

A cyclic compression–decompression pattern along the heart beat was observed (Fig. 9), namely the IMT was systematically maximal at the end of diastole, and minimal during systole, as described in the seminal work [42]. The mean $\mathcal{A}_{\mathrm{IMT}}$ (*i.e.*, the peak-to-peak amplitude of the wall's thickness temporal variation), was larger for the at-risk patients than for the control population. Although the mean difference (15 $\mu$m) between the two groups was on the same order of magnitude as the mean IMT segmentation uncertainty (22 $\mu$m), this difference was statistically significant with an "exploratory" $p$-value of 0.032. This finding is in accordance with previous studies [5, 27, 35, 36]. The compressibility of the arterial wall has been hypothesized to express fluid exchange and leakage between blood and wall layers [5], to reflect the wall's structural and mechanical alterations since the early stage of the pathology [27], and to have predictive power for outcomes [35]. We hypothesize that, during the atherosclerotic process, endothelial function is affected by the increased radial stress on the wall's innermost layers. The latter is reflected by a higher rate of compressibility, which could be observed with US imaging in this study.

As previously mentioned, integrating the distance between the LI and MA contours over the full exploitable width of each frame sometimes fails to capture a cyclic and reproducible compression–decompression temporal variation of the IMT. One possible explanation would be that this variation is not identical along the artery. Another possibility is that the segmentation uncertainties in relatively poorly contrasted parts of the wall included within the

width $W$ mask actual tiny variations. These hypotheses need to be verified.
A 3-year follow-up study is currently being conducted by our team, aiming to investigate the relationship between vascular health in subjects with either metabolic syndrome or type 1 or 2 diabetes, and the parameters that can be inferred from the curves provided by our method. Further application of this segmentation method to other peripheral arteries, such as humeral, popliteal, and brachial arteries, could also provide additional information about vascular health, as suggested by previous work [18, 49]. Future work will also focus on further automating the entire process, including the detection of diastole/systole, as well as a surface fitting approach in a 2D+t volume [28].

## 4.3 Limitations

As initially specified, this method was devised to segment the arterial wall in the absence of perceptible plaque. It can easily cope with a thickened wall, provided that the thickening is homogeneous along the artery. Indeed, the filter bank was designed to accommodate slight variations in IMT ($\pm 90\,\mu$m) around the value resulting from interactive initialization. It is likely to accommodate larger variations by increasing the $K$ parameter, but this increase may become contradictory with the smoothness assumption underlying the dynamic programming part of the method. Accuracy of the segmentation may further decrease in the presence of heterogeneous plaque, where more than two edges may be observed locally. However, such cases provide visual evidence of the disease, whereas our method was devised to assess the risk prior to plaque onset.
The temporal variation of the IMT during the heart beat was assessed within a single narrow region with visually best image quality for each sequence. The impact of choosing a different region was not assessed in this work. Reference curves were also missing to evaluate the accuracy of $\mathcal{A}_{\mathrm{IMT}}$, as collecting manual annotations to build such reference curves would be even more labor-consuming then constructing the reference to evaluate the segmentation process.
In this study, all sequences were acquired with the same US scanner, with the same protocol and settings, and by the same medical doctor. For this reason, the variability in image properties was solely due to inter-subject variability, that is to say the position, shape and orientation of the arterial walls in the image plane varying from one subject to another, whereas the image quality depended on the subjects' echogenicity. The use of a different acquisition setting and/or of a different US scanner may modify the overall image appearance. There are few parameters in our method (Section 2.6) and they could be tuned to accommodate such changes. All are related to pixel size (*e.g.*, $L$ and $l$) and these can only be adjusted to the scanner's actual spatial resolution. However, as long as the typical double-edge structure of the intima–media complex remains visible, as is the case in the vast majority of medical B-mode US images, we expect our method to be applicable. Further work involving various ultrasound devices as well as various acquisition settings would be necessary to assess the actual robustness of the method, but this was beyond of the scope of the present study. Generally, we recommend configuring the scanner's overall gain, central frequency, and focal zone so that both interfaces of the distal intima–media complex are clearly perceived during image acquisition. As for the temporal definition, the frame rate should be high enough to accurately capture the different phases of the cardiac cycle. It should also be emphasized that in its initial assumption, our method was not devised to process images with already developed thick heterogeneous plaque, and therefore might not provide segmentation results at the same accuracy level in such patients.
Two very different populations were involved in this study, namely younger healthy controls

and older diabetic patients at high cardiovascular risk. Therefore, we did not measure the influence of the pathology *per se* on the $\mathcal{A}_{\mathrm{IMT}}$ parameter. However, this proof of concept permitted us to quantify the accuracy of our method in subjects whose images varied in quality, as well as to confirm that a significant difference could be detected in the IMT compression between the two groups.
A 3-year follow-up study is currently being conducted by our team, aiming to investigate the relationship between vascular health in subjects with either metabolic syndrome or type 1 or 2 diabetes, and the parameters that can be inferred from the curves provided by our method. Further application of our segmentation method on other peripheral arteries, such as humeral, popliteal, and brachial arteries, could also provide additional information on vascular health, as suggested by previous work [18, 49]. Future work will also focus on further automating the entire process, including the detection of diastole/systole, as well as a surface fitting approach in a 2D+t volume [28].

### 4.4 Conclusion

We have presented a contour extraction method devised to localize the lumen–intima and media–adventitia interfaces of the CCA in US B-mode imaging. By combining a novel filter bank with an appropriate dynamic programming strategy, the method successfully copes with the local contrast drop that is locally observed along these interfaces. It provided reproducible, robust, and accurate results, in a reasonable computational time, for clinical images of variable geometry and/or quality. By successively processing all frames of a sequence, the temporal variation of the IMT during the heart beat can be assessed. Evaluated *in vivo* on 82 subjects, this novel method provided results as accurate as those obtained by experienced observers and showed greater reproducibility. Additionally, we observed that $\mathcal{A}_{\mathrm{IMT}}$, namely the amplitude of the IMT variation during the cardiac cycle, was significantly increased in at-risk patients w.r.t. healthy controls, which corroborates preliminary observations from the literature.

## Acknowledgements

This work was done within the French ANR Labex PRIMES and CeLyA. The authors would like to thank Dr. ir. Theo van Walsum, Dr. ir. Stefan Klein, and Dr. Aad van der Lugt for their valuable suggestions when proofreading the manuscript.

## Conflict of interest

The authors declare that they have no conflict of interest.

# Figures

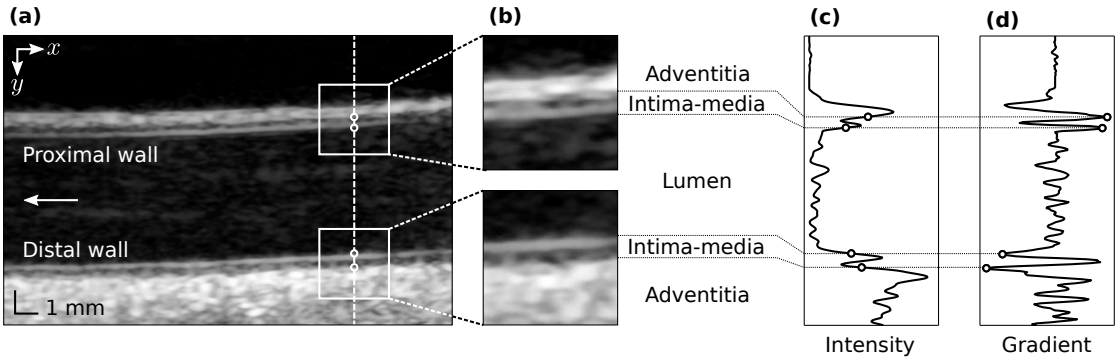


Figure 1: Representative example of a healthy common carotid artery acquired in ultrasound B-mode imaging. (a) Single frame, displaying both proximal and distal walls, encompassing the lumen. The characteristic structure pattern of each wall, consisting of two nearly parallel lines, is clearly visible. The blood flow direction is indicated by the white arrow. (b) Detailed regions, showing the different anatomical layers of the wall. (c) Radial intensity profile, corresponding to the dashed line in (a). The transition between the different layers is clearly visible. (d) Gradient of the intensity profile. The locations of the lumen–intima and media–adventitia interfaces correspond to the two maximum positive values for the proximal wall and the two minimum negative values for the distal wall (circles). All measurements and analyses reported in this article were conducted on the distal wall.

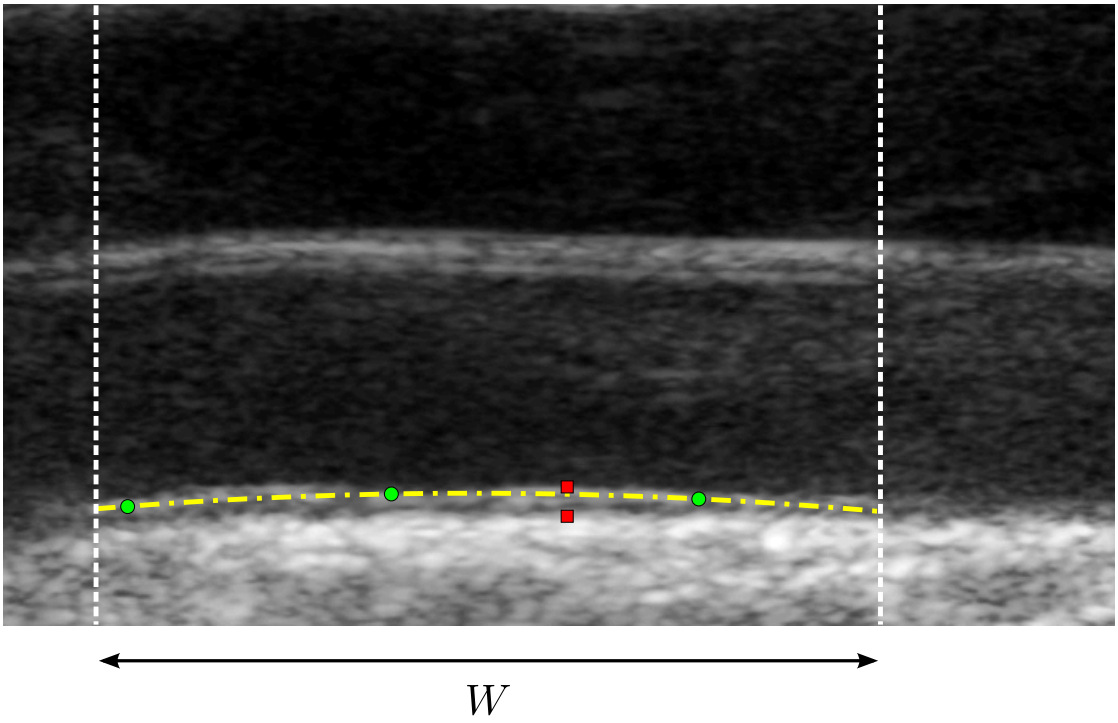


Figure 2: Schematic example of the user interaction performed during the segmentation initialization phase in the image $\mathcal{I}(1)$. First, the left and right borders are clipped out (vertical dashed lines), where the interfaces of the intima–media complex are not perceptible, thus defining the sub-image $\mathcal{I}_W$ of width $W$. Second, the approximate IMT value is determined (two red squares). Finally, the approximate position and curvature of the wall is determined (three green circles). The initial skeleton is determined by spline interpolation from the position of the three points (yellow line).

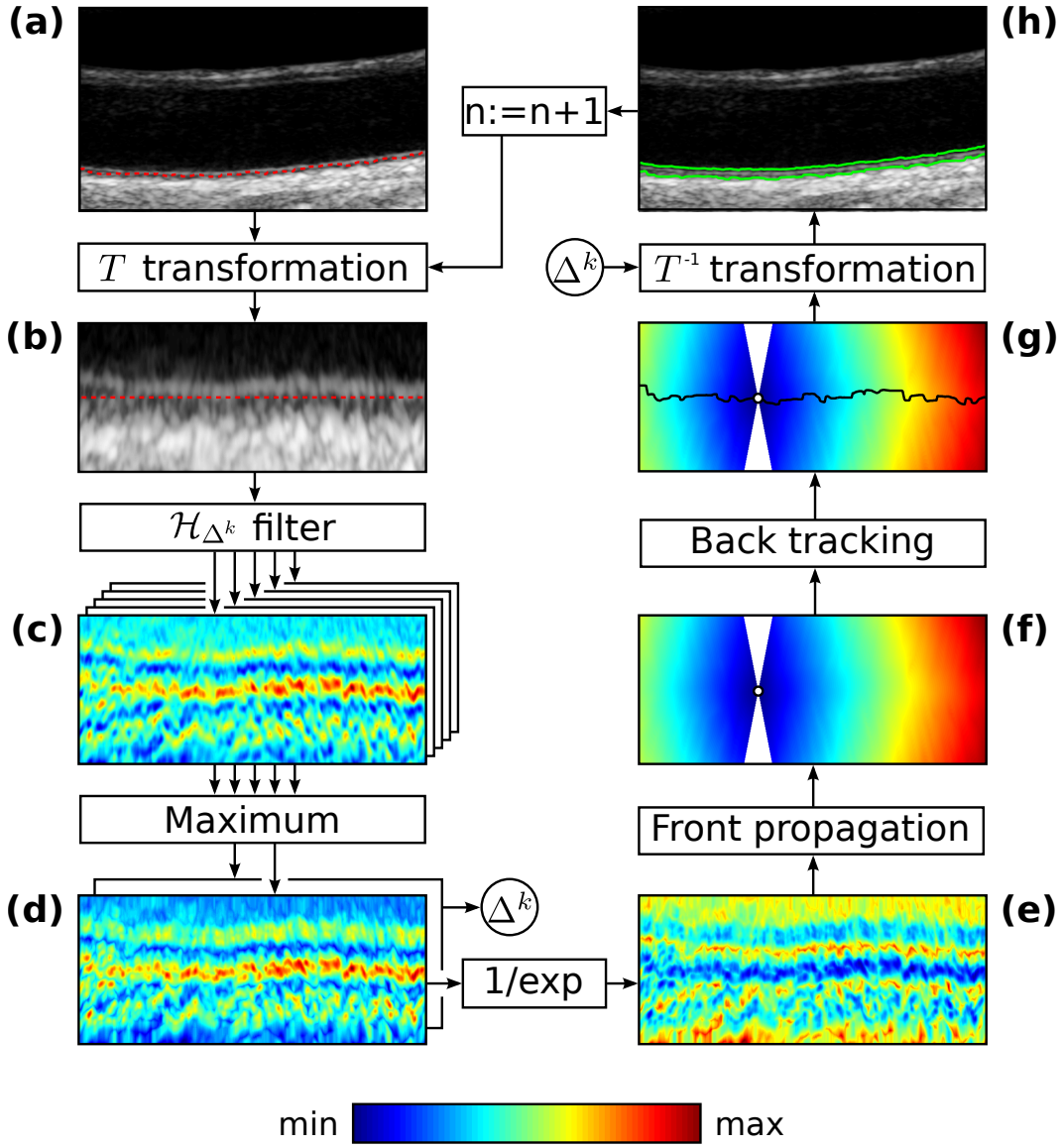


Figure 3: Sequential segmentation process (applied here to the full width of an image, *i.e.*, $\mathcal{I}_W = \mathcal{I}$ in this example). (a) Longitudinal B-mode image $\mathcal{I}(n)$ of the carotid artery and skeleton of the previous image (red dashes). (b) Sub-image $\mathcal{I}_T(n)$ resulting from the $T$ transformation, such that the interfaces of the distal wall around the previous skeleton (red dashes) are nearly horizontal. (c) Set of $K$ velocity maps $\mathrm{F}_{\Delta^k}$ created with the convolution operators $\mathcal{H}_{\Delta^k}$. (d) Maximal velocity map F and storage of the corresponding $\Delta^k$ local values. (e) Cost map C. (f) Cumulated cost map $\mathcal{C}$ generated from the seed (white dot). (g) Optimal path (black line) corresponding to the skeleton of the contours. (h) Final segmentation of the interfaces in $\mathcal{I}(n)$ (green lines), obtained from the central skeleton and the local IMT $\Delta^k$ values, after the inverse spatial transformation $T^{-1}$.

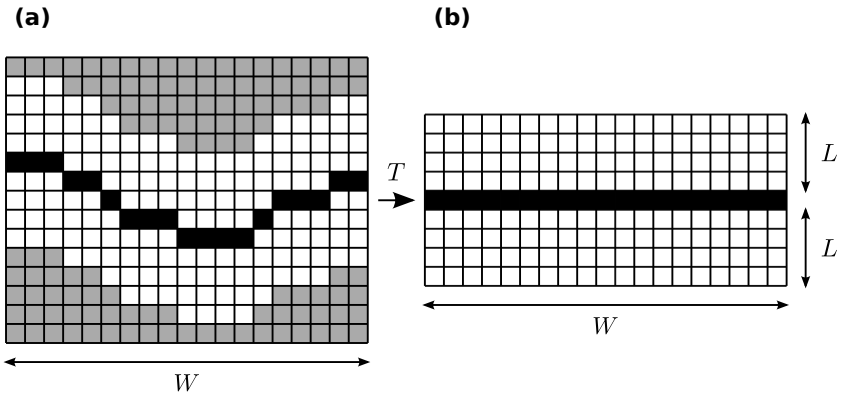


Figure 4: Spatial transformation $T$. (a) Original image $\mathcal{I}_W(n)$ and position of the skeleton from the previous image $\mathcal{I}_W(n-1)$ (black line). (b) Transformed image $\mathcal{I}_T$, generated by selecting, for each column, $L$ pixels below and above the skeleton, as depicted by the white squares in (a).

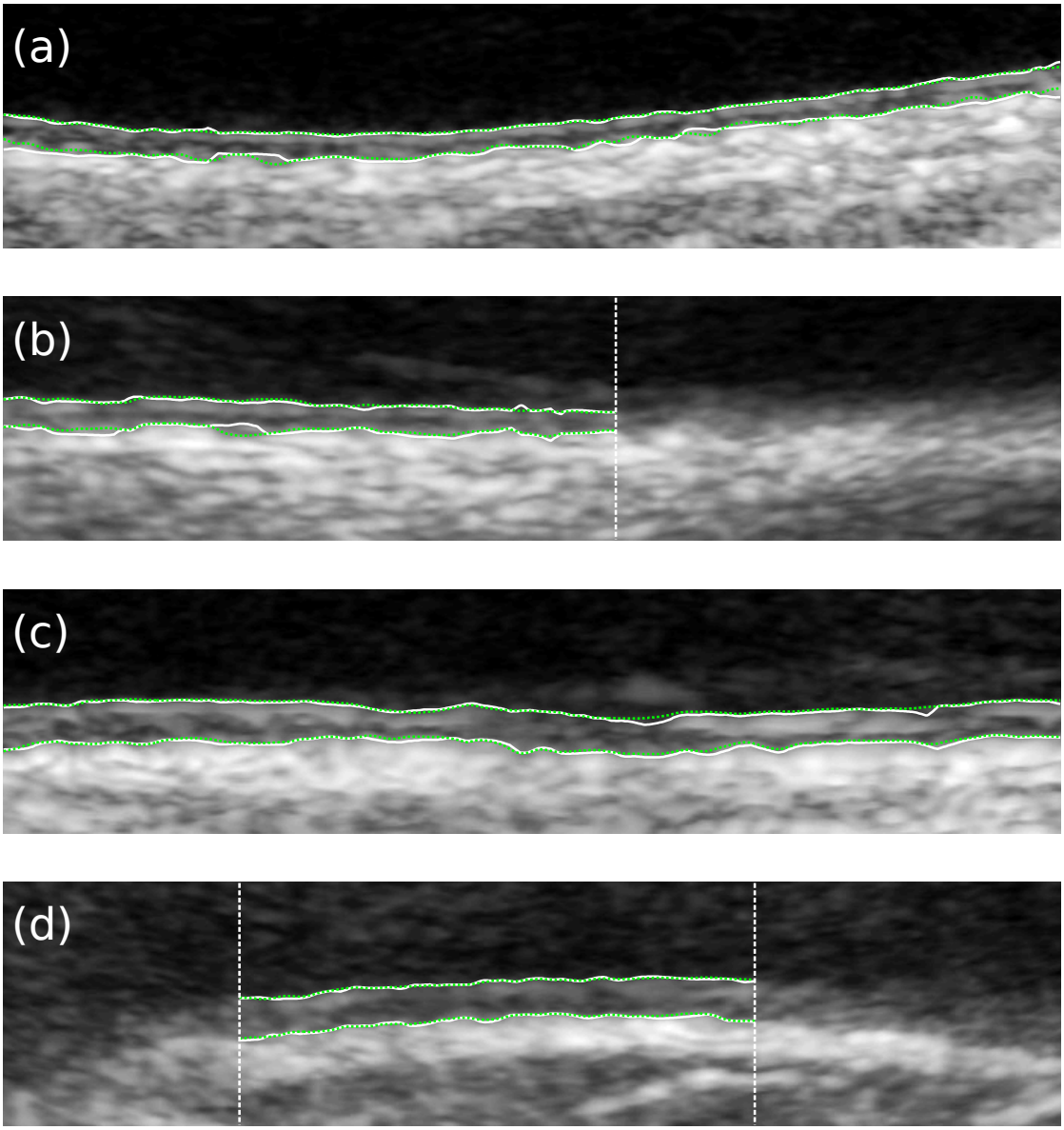


Figure 5: Results of our segmentation method (white solid lines), from two healthy volunteers (a, b) and two at-risk patients (c, d), compared to the reference (green dotted lines). The left and/or right borders presenting poor image quality have been clipped out (vertical lines) prior to segmenting the contours.

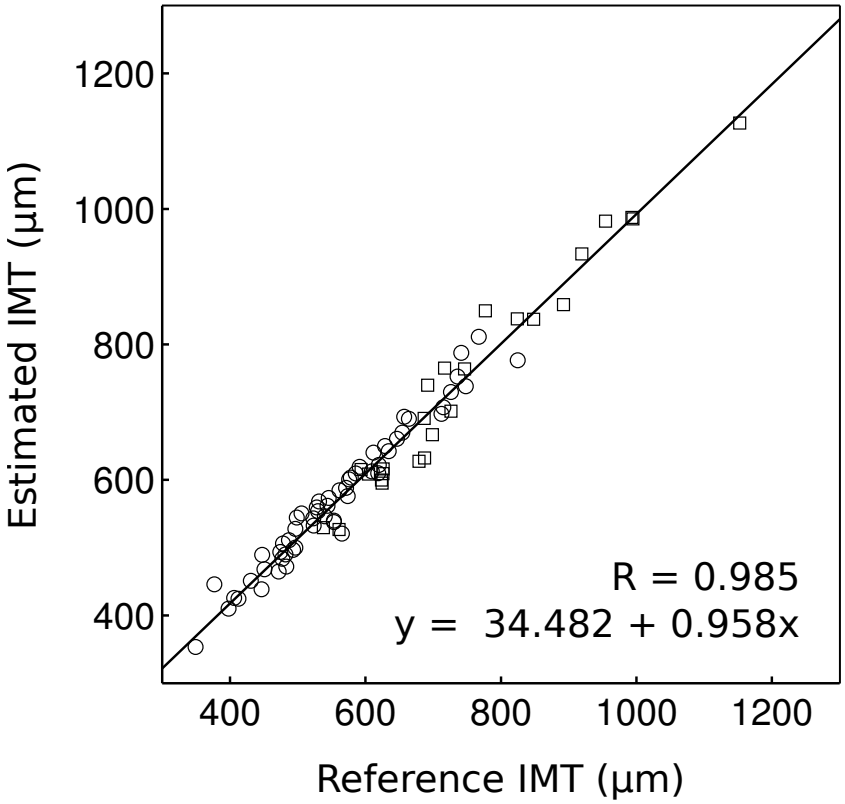


Figure 6: Linear regression line and correlation coefficient $R$ between the reference IMT value and the estimation performed by our segmentation method in the first image of each sequence, for healthy volunteers (circles) and at-risk patients (squares).

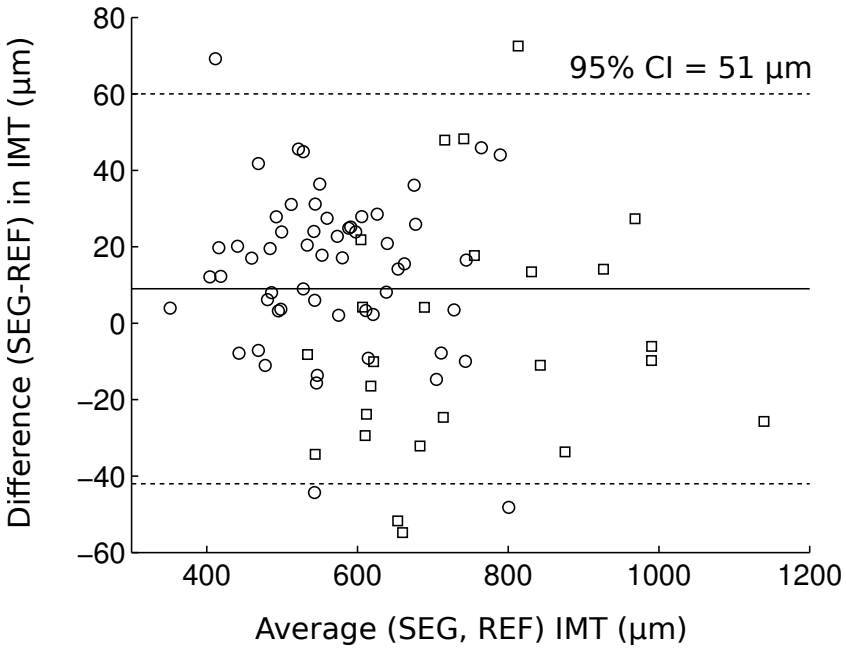


Figure 7: Bland-Altman plot comparing the IMT value estimated by our method (SEG) in the first image of each sequence with the reference (REF), for healthy volunteers (circles) and at-risk patients (squares).

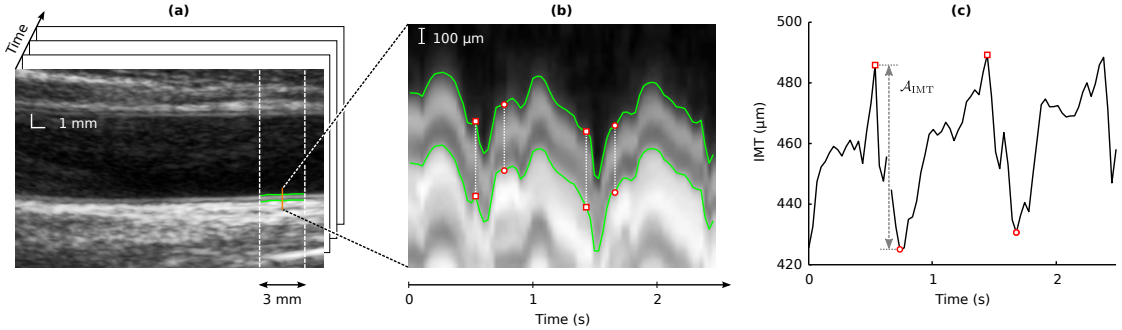


Figure 8: Variation of the intima–media thickness (IMT) during the cardiac cycle. (a) Segmentation of the intima–media complex, on a local region of reduced width ($W = 3\,\mathrm{mm}$). (b) Successive positions of the lumen–intima and media–adventitia interfaces during the sequence, for a single column corresponding to the orange vertical bar in (a). The end-diastole and the systole are depicted by the square and circular markers, respectively. (c) Corresponding variation of the IMT and peak-to-peak magnitude used to calculate the parameter $\mathcal{A}_{\mathrm{IMT}}$.

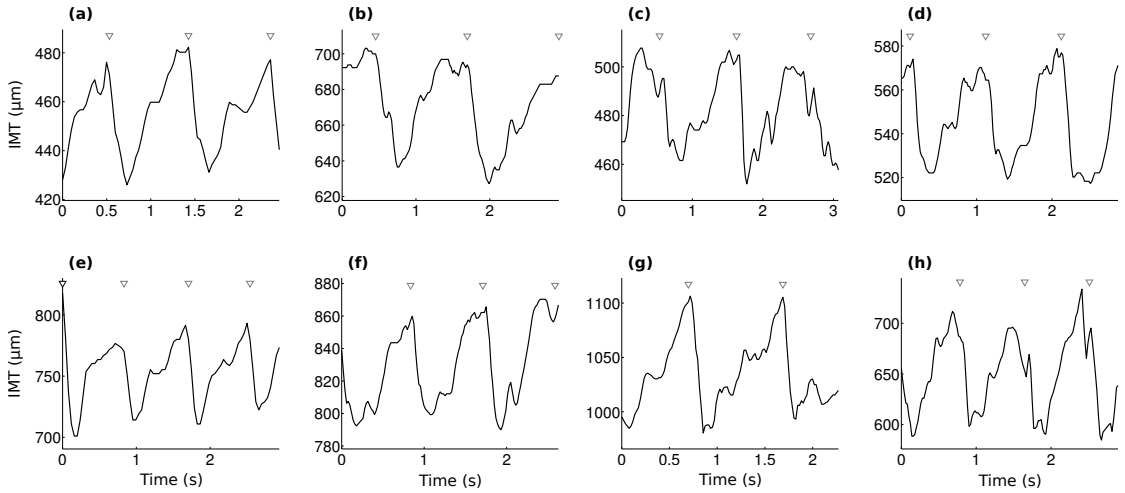


Figure 9: Temporal variation of the intima–media thickness (IMT) during several cardiac cycles, resulting from our segmentation method, for four healthy volunteers (a–d) and four at-risk patients (e–h). The end of the diastole is indicated by the triangle markers.

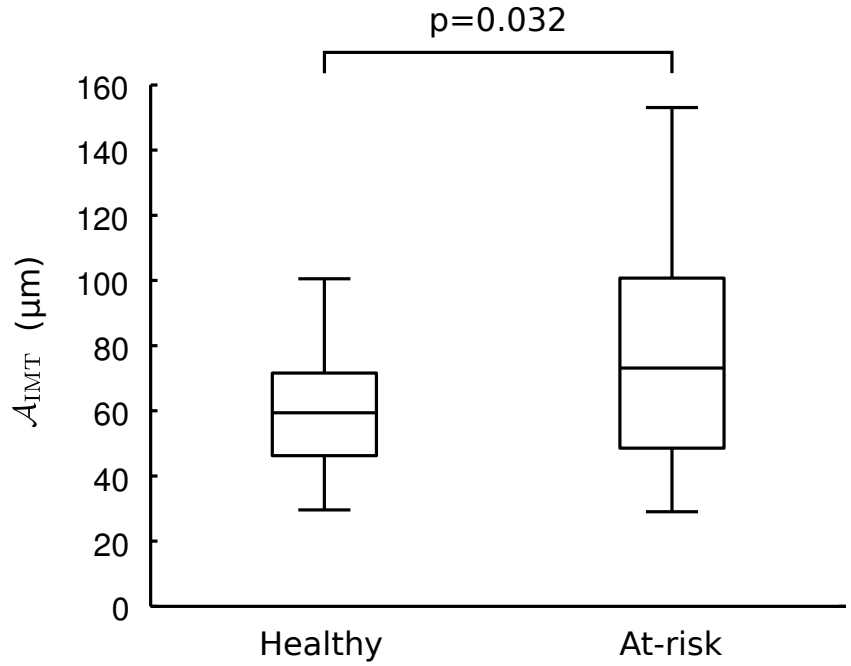


Figure 10: Box plot representing the variation amplitude of the intima–media complex ($\mathcal{A}_{\mathrm{IMT}}$) during the cardiac cycle, for healthy volunteers and at-risk patients. Percentiles are indicated by boxes (25th and 75th), inner lines (50th) and error bars (5th and 95th). The result of the Mann-Whitney U test is indicated by the $p$-value.

# Tables

Table 1: Segmentation absolute errors as well as bias (mean ± standard deviation) in $\mu$m, for our computerized method (SEG) and the manual tracings ($O_{1,2,3}$).

| Method | lumen–intima interface | media–adventitia interface | intima–media thickness |
|---|---|---|---|
| | Healthy volunteers (n=57) | | |
| SEG *vs* Reference | 29 ± 25 | 41 ± 38 | 21 ± 15 |
| SEG variability | 8 ± 17 | 13 ± 39 | 9 ± 12 |
| Inter-observer variability | 46 ± 41 | 40 ± 39 | 49 ± 37 |
| Intra-observer variability | 32 ± 33 | 32 ± 40 | 29 ± 26 |
| | At-risk patients (n=25) | | |
| SEG *vs* Reference | 30 ± 30 | 43 ± 40 | 26 ± 18 |
| SEG variability | 18 ± 22 | 20 ± 27 | 11 ± 21 |
| Inter-observer variability | 31 ± 29 | 40 ± 41 | 37 ± 28 |
| Intra-observer variability | 24 ± 30 | 32 ± 43 | 24 ± 25 |
| | All subjects (n=82) | | |
| SEG *vs* Reference | 29 ± 27 | 42 ± 38 | 22 ± 16 |
| SEG variability | 11 ± 19 | 15 ± 36 | 9 ± 15 |
| Inter-observer variability | 41 ± 38 | 40 ± 40 | 46 ± 35 |
| Intra-observer variability | 30 ± 32 | 32 ± 41 | 27 ± 25 |
| SEG bias | 9 ± 39 | 18 ± 54 | 9 ± 26 |
| $O_1$ bias | -1 ± 30 | 17 ± 32 | 17 ± 29 |
| $O_2$ bias | 18 ± 31 | -10 ± 31 | -28 ± 27 |
| $O_3$ bias | -17 ± 27 | -6 ± 28 | 11 ± 24 |

# References


[1] Baldassarre, D., Amato, M., Bondioli, A., Sirtori, C.R., Tremoli, E.: Carotid artery intima-media thickness measured by ultrasonography in normal clinical practice correlates well with atherosclerosis risk factors. Stroke **31**(10), 2426–2430 (2000)

[2] Bellman, R.: Dynamic programming. Science **153**(3731), 34–37 (1966)

[3] Bland, J.M., Altman, D.G.: Statistical methods for assessing agreement between two methods of clinical measurement. The Lancet **327**(8476), 307–310 (1986)

[4] Bots, M.L., Hoes, A.W., Koudstaal, P.J., Hofman, A., Grobbee, D.E.: Common carotid intima-media thickness and risk of stroke and myocardial infarction: The Rotterdam Study. Circulation **96**(5), 1432–1437 (1997)

[5] Boutouyrie, P., Germain, D.P., Tropeano, A.I., Laloux, B., Carenzi, F., Zidi, M., Jeunemaitre, X., Laurent, S.: Compressibility of the carotid artery in patients with pseudoxanthoma elasticum. Hypertension **38**(5), 1181–1184 (2001)

[6] Burke, G.L., Evans, G., Riley, W.A., Sharrett, A.R., Howard, G., Barnes, R.W., Rosamond, W., Crow, R.S., Rautaharju, P.M., Heiss, G.: Arterial wall thickness is associated with prevalent cardiovascular disease in middle-aged adults: The Atherosclerosis Risk in Communities (ARIC) Study. Stroke **26**(3), 386–391 (1995)

[7] Celermajer, D.S., Sorensen, K.E., Gooch, V.M., Sullivan, I.D., Lloyd, J.K., Deanfield, J.E., Spiegelhalter, D.J.: Non-invasive detection of endothelial dysfunction in children and adults at risk of atherosclerosis. The Lancet **340**(8828), 1111–1115 (1992)

[8] Cheng, D.C., Jiang, X.: Detections of arterial wall in sonographic artery images using dual dynamic programming. IEEE Transactions on Information Technology in Biomedecine **12**(6), 792–799 (2008)

[9] Cheng, D.C., Schmidt-Trucksäss, A., Cheng, K., Burkhardt, H.: Using snakes to detect the intimal and adventitial layers of the common carotid artery wall in sonographic images. Computer Methods and Programs in Biomedicine **67**(1), 27–37 (2002)

[10] Cinthio, M., Jansson, T., Ahlgren, Å.R., Lindström, K., Persson, H.W.: A method for arterial diameter change measurements using ultrasonic B-mode data. Ultrasound in Medecine & Biology **36**(9), 1504–1512 (2010)

[11] Cinthio, M., Jansson, T., Persson, H.W., Lindstrom, K., Ahlgren, Å.R.: New non-invasive method for intima-media thickness and intima-media compression measurements. In: IEEE International Ultrasonics Symposium, vol. 1, pp. 385–388. Rotterdam, Netherlands (2005)

[12] Cohen, L.: Minimal paths and fast marching methods for image analysis. Mathematical Models in Computer Vision: The Handbook pp. 97–111 (2005)

[13] Delsanto, S., Molinari, F., Giustetto, P., Liboni, W., Badalamenti, S., Suri, J.S.: Characterization of a completely user-independent algorithm for carotid artery segmentation in 2-D ultrasound images. IEEE Transactions on Instrumentation and Measurement **56**(4), 1265–1274 (2007)

[14] Destrempes, F., Meunier, J., Giroux, M.F., Soulez, G., Cloutier, G.: Segmentation in ultrasonic B-mode images of healthy carotid arteries using mixtures of nakagami distributions and stochastic optimization. IEEE Transactions on Medical Imaging **28**(2), 215–229 (2009)

[15] Faita, F., Gemignani, V., Bianchini, E., Giannarelli, C., Ghiadoni, L., Demi, M.: Real-time measurement system for evaluation of the carotid intima-media thickness with a robust edge operator. Journal of Ultrasound in Medicine **27**(9), 1353–1361 (2008)

[16] Ford, E.S.: Risks for all-cause mortality, cardiovascular disease, and diabetes associated with the metabolic syndrome: a summary of the evidence. Diabetes Care **28**(7), 1769–1778 (2005)

[17] Ford, E.S., Ajani, U.A., Croft, J.B., Critchley, J.A., Labarthe, D.R., Kottke, T.E., Giles, W.H., Capewell, S.: Explaining the decrease in US deaths from coronary disease, 1980-2000. The New England journal of medicine **356**(23), 2388–2398 (2007)

[18] Gemignani, V., Faita, F., Ghiadoni, L., Poggianti, E., Demi, M.: A system for real-time measurement of the brachial artery diameter in B-mode ultrasound images. IEEE Transactions on Medical Imaging **26**(3), 393–404 (2007)

[19] Golemati, S., Stoitsis, J., Sifakis, E.G., Balkizas, T., Nikita, K.S.: Using the Hough transform to segment ultrasound images of longitudinal and transverse sections of the carotid artery. Ultrasound in Medecine & Biology **33**(12), 1918–1932 (2007)

[20] Haller, C., Schulz, J., Schmidt-Trucksäss, A., Burkardt, H., Schmitz, D., Dickhuth, H.H., Sandrock, M.: Sequential based analysis of Intima-Media Thickness (IMT) in common carotid artery studies. Atherosclerosis **195**(2), e203–e209 (2007)

[21] Ilea, D.E., Duffy, C., Kavanagh, L., Stanton, A., Whelan, P.F.: Fully automated segmentation and tracking of the intima media thickness in ultrasound video sequences of the common carotid artery. IEEE Transactions on Ultrasonics, Ferroelectrics and Frequency Control **60**(1), 158–177 (2013)

[22] Laurent, S., Boutouyrie, P., Asmar, R., Gautier, I., Laloux, B., Guize, L., Ducimetiere, P., Benetos, A.: Aortic stiffness is an independent predictor of all-cause and cardiovascular mortality in hypertensive patients. Hypertension **37**(5), 1236–1241 (2001)

[23] Lee, Y.B., Choi, Y.J., Kim, M.H.: Boundary detection in carotid ultrasound images using dynamic programming and a directional haar-like filter. Computers in Biology and Medicine **40**(8), 687–697 (2010)

[24] Liang, Q., Wendelhag, I., Wikstrand, J., Gustavsson, T.: A multiscale dynamic programming procedure for boundary detection in ultrasonic artery images. IEEE Transactions on Medical Imaging **19**(2), 127–142 (2000)

[25] Loizou, C.P., Pattichis, C.S., Pantziaris, M., Tyllis, T., Nicolaides, A.: Snakes based segmentation of the common carotid artery intima media. Medical & Biological Engineering & Computing **45**(1), 35–49 (2007)

[26] Lorenz, M.W., Markus, H.S., Bots, M.L., Rosvall, M., Sitzer, M.: Prediction of clinical cardiovascular events with carotid intima-media thickness: a systematic review and meta-analysis. Circulation **115**(4), 459–467 (2007)

[27] Meinders, J.M., Kornet, L., Hoeks, A.P.G.: Assessment of spatial inhomogeneities in intima media thickness along an arterial segment using its dynamic behavior. American Journal of Physiology-Heart and Circulatory Physiology **285**(1), H384–H391 (2003)

[28] Metz, C.T., Klein, S., Schaap, M., van Walsum, T., Niessen, W.J.: Nonrigid registration of dynamic medical imaging data using nD+t B-splines and a groupwise optimization approach. Medical Image Analysis **15**(2), 238–249 (2011)

[29] Molinari, F., Liboni, W., Giustetto, P., Badalamenti, S., Suri, J.S.: Automatic computer-based tracings (ACT) in longitudinal 2-D ultrasound images using different scanners. Journal of Mechanics in Medicine and Biology **9**(04), 481–505 (2009)

[30] Molinari, F., Zeng, G., Suri, J.S.: A state of the art review on intima-media thickness (IMT) measurement and wall segmentation techniques for carotid ultrasound. Computer Methods and Programs in Biomedicine **100**(3), 201–221 (2010)

[31] Molinari, F., Zeng, G., Suri, J.S.: Completely automated robust edge snapper for carotid ultrasound imt measurement on a multi-institutional database of 300 images. Medical & Biological Engineering & Computing **49**(8), 177–192 (2011)

[32] Nilsson, T., Ahlgren, Å.R., Jansson, T., Persson, H.W., Lindström, K., Nilsson, J., Cinthio, M.: A method for measuring the variation of intima-media thickness during the entire cardiac cycle using B-mode images. In: IEEE International Ultrasonics Symposium, pp. 2126–2129. Orlando, FL, USA (2011)

[33] O'Leary, D.H., Polak, J.F., Kronmal, R.A., Manolio, T.A., Burke, G.L., Wolfson, S.K.J.: Carotid-artery intima and media thickness as a risk factor for myocardial infarction and stroke in older adults. New England Journal of Medicine **340**(1), 14–22 (1999)

[34] Pannier, B., Guerin, A.P., Marchais, S.J., Metivier, F., Safar, M.E., London, G.M.: Postischemic vasodilation, endothelial activation, and cardiovascular remodeling in end-stage renal disease. Kidney International **57**(3), 1091–1099 (2000)

[35] Polak, J.F., Johnson, C., Harrington, A., Wong, Q., O'Leary, D.H., Burke, G., Yanez, N.D.: Changes in carotid intima-media thickness during the cardiac cycle: The multi-ethnic study of atherosclerosis. Journal of the American Heart Association **1**(4) (2012). DOI 10.1161/JAHA.112.001420

[36] Polak, J.F., Meisner, A., Pencina, M.J., Wolf, P.A., D'Agostino, R.B.: Variations in common carotid artery intima-media thickness during the cardiac cycle: implications for cardiovascular risk assessment. Journal of the American Society of Echocardiography **25**(9), 1023–1028 (2012)

[37] Rocha, R., Campilho, A., Silva, J., Azevedo, E., Santos, R.: Segmentation of the carotid intima-media region in B-mode ultrasound images. Image and Vision Computing **28**(4), 614–625 (2010)

[38] Rossi, A.C., Brands, P.J., Hoeks, A.P.G.: Automatic localization of intimal and adventitial carotid artery layers with noninvasive ultrasound: A novel algorithm providing scan quality control. Ultrasound in Medecine & Biology **36**(3), 467–479 (2010)

[39] Sandrock, M., Hansel, J., Schulze, J., Schmitz, D., Niess, A., Burkhardt, H., Schmidt-Trucksäss, A.: Sequentially based analysis versus image based analysis of Intima

Media Thickness in common carotid arteries studies – Do major IMT studies underestimate the true relations for cardio-and cerebrovascular risk? Cardiovascular Ultrasound **6**(32), 1–8 (2008)

[40] Schaar, J.A., Muller, J.E., Falk, E., Virmani, R., Fuster, V., Serruys, P.W., Colombo, A., Stefanadis, C., Ward, C.S., Moreno, P.R., Maseri, A., van der Steen, A.F.W.: Terminology for high-risk and vulnerable coronary artery plaques. Report of a meeting on the vulnerable plaque, June 17 and 18, 2003, Santorini, Greece. European Heart Journal **25**(12), 1077–1082 (2004)

[41] Selzer, R.H., Hodis, H.N., Kwong-Fu, H., Mack, W.J., Lee, P.L., Liu, C.R., Liu, C.H.: Evaluation of computerized edge tracking for quantifying intima-media thickness of the common carotid artery from B-mode ultrasound images. Atherosclerosis **111**(1), 1–11 (1994)

[42] Selzer, R.H., Mack, W.J., Lee, P.L., Kwong-Fu, H., Hodis, H.N.: Improved common carotid elasticity and intima-media thickness measurements from computer analysis of sequential ultrasound frames. Atherosclerosis **154**(1), 185–193 (2001)

[43] Sethian, J.A.: A fast marching level set method for monotonically advancing fronts. Proceedings of the National Academy of Sciences **93**(4), 1591–1595 (1996)

[44] Teynor, A., Caviezel, S., Dratva, J., Künzli, N., Schmidt-Trucksäss, A.: An automated, interactive analysis system for ultrasound sequences of the common carotid artery. Ultrasound in Medicine & Biology **38**(8), 1440–1450 (2012)

[45] Trawiński, Z.: Ultrasonic method for relative changes of intima-media thickness measurements in common carotid artery. Hydroacoustics Selected full texts **11**, 411–418 (2008)

[46] Trawiński, Z., Powałowski, T.: Modeling and ultrasonic examination of common carotid artery wall thickness changes. Archives of Acoustics **31**, 29–34 (2006)

[47] Wijeysundera, H.C., Machado, M., Farahati, F., Wang, X., Witteman, W., van der Velde, G., Tu, J.V., Lee, D.S., Goodman, S.G., Petrella, R., O'Flaherty, M., Krahn, M., Capewell, S.: Association of temporal trends in risk factors and treatment uptake with coronary heart disease mortality, 1994-2005. JAMA: the Journal of the American Medical Association **303**(18), 1841–1847 (2010)

[48] Wikstrand, J.: Methodological considerations of ultrasound measurement of carotid artery intima–media thickness and lumen diameter. Clinical Physiology and Functional Imaging **27**(6), 341–345 (2007)

[49] Woodman, R.J., Playford, D.A., Watts, G.F., Cheetham, C., Reed, C., Taylor, R.R., Puddey, I.B., Beilin, L.J., Burke, V., Mori, T.A., Green, D.: Improved analysis of brachial artery ultrasound using a novel edge-detection software system. Journal of Applied Physiology **91**(2), 929–937 (2001)

[50] Zahnd, G., Vray, D., Sérusclat, A., Alibay, D., Bartold, M., Brown, A., Durand, M., Jamieson, L.M., Kapellas, K., Maple-Brown, L.J., O'Dea, K., Moulin, P., Celermajer, D.S., Skilton, M.R.: Longitudinal displacement of the carotid wall and cardiovascular risk factors: associations with aging, adiposity, blood pressure and periodontal disease independent of cross-sectional distensibility and intima-media thickness. Ultrasound in Medecine & Biology **38**(10), 1705–1715 (2012)